Aerogel-based collection of ejecta material from asteroids from libration point orbits: Dynamics and capture design

Carlo Burattini, Camilla Colombo (✉), and Mirko Trisolini

Department of Space Science and Technology, Politecnico di Milano, via La Masa 34, Milan 10156, Italy

ABSTRACT

Scientific interest in asteroids and their physical characteristics is growing. These bodies provide insights into the primordial solar system and represent a valuable source of metals, silicates, and water. Several missions over the past few years have aimed to improve and better identify the main properties of these poorly known celestial bodies. However, these missions relied on touchdown(s) on the target asteroid to gather samples, which is complicated owing to the difficulty of accurately reaching and rendezvousing with the body. This study aims to assess the feasibility of an in-orbit asteroid sample collection mission. Such a strategy could prevent complex operations related to landing and touchdown maneuvers and avoid the dead times present in a mission requiring several landings. The presented collection scenario, which focuses on the asteroid Ryugu, proposes gathering samples using a spacecraft injected into a halo orbit around the second libration point, L_2. For this purpose, the orbits in the neck region of the zero velocity curves are analyzed. A novel methodology to characterize bouncing behavior is introduced. An interpolation-based approach was used to recover the appropriate restitution coefficients for each collision occurring at a specific impact angle. This was applied to both the rigid body model and the point mass approximation studied for two different sites on the asteroid. Furthermore, the study enlarged the region of interest from only L_2 to its neighboring zones to return a more global and realistic point of view. Considering the solar radiation pressure and asteroid aspherical potential, particles of different sizes ejected from different longitudes and with different ejection angles were classified according to their trajectories to finally build a database. Based on this analysis, an aerogel-based collection strategy inspired by that used in the Stardust-NExT (NASA) mission was investigated to assess its possible applicability to the analyzed scenario.

KEYWORDS

three-body problem
ejecta dynamics
bouncing behavior
libration point orbits
asteroid sample collection
aerogel capture

Research Article

Received: 16 May 2023
Accepted: 25 December 2023

1 Introduction

Asteroids provide fundamental information about the early solar system and its evolution. They are also a valuable source of metals, silicates, and water that is potentially exploitable for in situ resource utilization (ISRU) [1, 2]. In recent years, several missions, such as Deep Impact (NASA), OSIRIS-REx (NASA), Hayabusa, and Hayabusa2 (JAXA) [3], have carried out efforts aimed at determining and characterizing the as-yet poorly known properties of asteroids. Moreover, these celestial bodies open up the possibility of conducting space exploration at a reasonable cost, representing perfect targets for future space achievements [4]. Furthermore, asteroid exploration is a key factor in mitigating their impact risk, and improving our knowledge of the properties of asteroids will lead to an increased efficiency of asteroid deflection techniques to enable planetary protection in the event of a possible collision. The

✉ camilla.colombo@polimi.it

importance of such techniques was highlighted by the NASA's Dart mission [5], which proved that the path of an asteroid can be changed by an impactor hitting the celestial body.

In this study, we investigated the possibility of performing sample collection in orbit. Specifically, we studied the feasibility of sample collection by a satellite orbiting around the second libration point, L_2. Assessing the feasibility of an in-orbit collection strategy can be beneficial, as it can help prevent complex operations related to landing and touchdown maneuvers and also avoid all dead times present in a mission requiring several landings.

Trisolini *et al.* [6] compared sample collection at L_2 with the collection of orbiting particles prior to their re-impact. For the former, which is also the subject of this study, the region of interest was broadened relative to L_2 itself, and re-impact and bouncing behaviors were introduced. This strategy was partially investigated by Villegas-Pinto *et al.* [7]. Their study focused on assessing the impact location, particle radius, and ejection velocity leading to particle capture in periodic orbits around an asteroid. Although this work provides some useful insights into the capture strategy, it is directed toward collision-related hazards rather than the capture itself, taking a more general view of the fate of ejecta and studying re-impacts and escapes. Latino *et al.* [8] investigated the dynamics arising from the re-impact and bouncing of particles ejected from an asteroid to analyze the potential threat of captured particles. The bouncing behavior was studied using a novel methodology that calculates the coefficients of restitution through interpolation.

Taking the work of Kikuchi *et al.* [9] as the starting point, we studied the bouncing behavior of the ejected particles, considering the restitution coefficients estimated by Mission Hayabusa2. We also assessed the possibility of particles being injected again into the orbit after bouncing. Finally, a preliminary design of the capture mechanism to be mounted on an orbiting spacecraft was tested, highlighting the advantages and disadvantages of the presented solution. The design relies on an aerogel panel based on the one used in the Stardust-NExT mission (NASA) and uses the relations for hypervelocity impacts developed in the literature. The percentage of the aerogel-exposed surface with respect to the entire area of one of the aerogel panels and the preliminary values of the panel's thickness and area were estimated.

In this study, the reference scenario is the asteroid Ryugu, whose main properties are listed in Table 1. Soldini and Tsuda [10] reported that Hayabusa2, during its mission on Ryugu, needed to wait for up to two weeks between one operation and the next one because of the time required for the dissipation of the ejecta plume, which is mandatory to ensure a safe landing of the spacecraft. However, in our study, we sought to understand whether the presence of orbiting ejecta could be exploited and leveraged to increase the sample collection capabilities of the spacecraft.

Table 1 Main properties of Ryugu

Property	Value
Rotational period	7.631 h
Orbital period	1.3 years
Effective radius	440 m
Ellipsoid axis	$a = 446.5$ m; $b = 439.7$ m; $c = 433.9$ m
μ_a	32 m^3/s^2
Density (bulk)	1282 kg/m^3
Mass	$(4.50 \pm 0.06) \times 10^{11}$ kg

2 Dynamical model

To study the Sun–Ryugu system, the motion of the asteroid's ejecta was modeled using the three-body problem. Let m_S, m_R, and $m_{S/C}$ be the masses of the Sun, Ryugu, and the spacecraft, respectively. Then, $m_S > m_R \gg m_{S/C}$ (i.e., the third body can be considered a "mass-less" object). Assuming that the primaries follow circular paths, the problem can be studied within the circular restricted three-body problem (CR3BP) approximation. The main perturbations affecting CR3BP dynamics can then be identified following Gustafson [11], according to whom the gravity, pressure forces, and electromagnetic Lorentz forces are proportional to s^3, s^2, and s, respectively, where s is the radius of a particle. This means that the electromagnetic forces can usually be neglected. Therefore, we only consider solar radiation and aspherical harmonic gravitational perturbations. The effect of the solar radiation pressure (SRP) was considered by using a cannon-ball model, as in Soldini [12]. Following this approximation, the force owing to solar radiation always acts in the direction opposite to that of the Sun. In addition, because it is dependent only on the spacecraft–Sun distance, it can be treated as a conservative force,

which can be described by a potential [6, 13]. The key parameter is the lightness parameter β, which is defined as the ratio of the SRP acceleration to the solar gravity acceleration and is obtained using Eq. (1) [14], where AU is the astronomic unit ($= 1.496 \times 10^8$ km), P_0 is the solar flux at 1 AU ($= 1367$ W/m^2), c_R is the particle reflectivity coefficient, ρ_P is the particle density, and r_P is the particle diameter.

$$\beta = P_0 \frac{\mathrm{AU}^2}{\mu_\mathrm{Sun}} \frac{3c_\mathrm{R}}{2\rho_\mathrm{p} r_\mathrm{p}} \tag{1}$$

As Ryugu is a spinning top-shaped asteroid, the potential perturbation is aspherical, presenting a pronounced equatorial bulge and symmetrical shape. These characteristics can be described by the J_2 aspherical potential term. Therefore, for the purposes of this study, we considered it to approximate Ryugu's gravitational field. The value of J_2 can be estimated from Ryugu's mean radius and axis (as reported in Table 1), and in this case, $J_2 = 0.008347066115702$ [14].

Following the usual procedure, we then adimensionalize the problem by taking:

- the reference mass, $M_\mathrm{ref} = m_\mathrm{S} + m_\mathrm{R}$;
- the reference length, l_ref, equal to the Sun–Ryugu distance, i.e., $l_\mathrm{ref} = 1.19$ AU;
- the time unit τ such that the angular rate of the three-body system is unity (i.e., $\Omega = 1$).

The equations of motion, expressed in a synodic frame, therefore become those stated in Eq. (2) [14], where $\mu = m_\mathrm{R}/M_\mathrm{ref}$, $\bar{a} = R_\mathrm{Ryugu}/l_\mathrm{ref}$, and $\bar{n}^2 = 1+(3/2)J_2\bar{a}^2$, while the terms r_sp and r_ap, representing the Sun–particle and Ryugu–particle distances, respectively, can be computed as $r_\mathrm{sp} = [(x+\mu)^2 + y^2 + z^2]^{1/2}$ and $r_\mathrm{ap} = [(x+\mu-1)^2 + y^2 + z^2]^{1/2}$. The synodic frame adopted is a cartesian reference frame, which rotates at the same rate as the three-body system and is centered at the center of mass of the system itself. Thus, the coordinates x, y, and z are the distances of a particle from the center of mass of the system: the x-axis is directed toward the smaller primary, the z-axis is along the angular momentum vector, and the y-axis completes a right-handed triad.

However, the formulation shown in Eq. (2) is only possible because Ryugu's spin axis is oriented approximately normal to the orbital plane [15], leading to an easier derivation when considering J_2.

Furthermore, Eq. (2) underlines how, when considering the SRP, that is, when $\beta \neq 0$, the dynamics of a particle will be strongly dependent on its dimensions. Specifically, ejecta are naturally sorted according to their size owing to the action of solar radiation (the larger the grain, the lower the value of β). Therefore, the SRP can be used as a passive in situ mass spectrometer [16]. This aspect is crucial for assessing the dimensions of the particles that will be gathered during a collection mission.

$$\begin{cases} \ddot{x} - 2\bar{n}\dot{y} = \bar{n}^2 x - \dfrac{(1-\beta)(1-\mu)(x+\mu)}{r_\mathrm{sp}^3} \\ \quad - \dfrac{\mu}{r_\mathrm{ap}^3}\left[1 - \dfrac{3}{2}J_2\left(\dfrac{\bar{a}}{r_\mathrm{ap}}\right)^2\left(5\dfrac{z^2}{r_\mathrm{ap}^2} - 1\right)\right](x+\mu-1) \\ \ddot{y} + 2\bar{n}\dot{x} = \bar{n}^2 y - \dfrac{(1-\beta)(1-\mu)}{r_\mathrm{sp}^3} y \\ \quad - \dfrac{\mu}{r_\mathrm{ap}^3}\left[1 - \dfrac{3}{2}J_2\left(\dfrac{\bar{a}}{r_\mathrm{ap}}\right)^2\left(5\dfrac{z^2}{r_\mathrm{ap}^2} - 1\right)\right] y \\ \ddot{z} = -\dfrac{(1-\beta)(1-\mu)}{r_\mathrm{sp}^3} z \\ \quad - \dfrac{\mu}{r_\mathrm{ap}^3}\left[1 - \dfrac{3}{2}J_2\left(\dfrac{\bar{a}}{r_\mathrm{ap}}\right)^2\left(5\dfrac{z^2}{r_\mathrm{ap}^2} - 3\right)\right] z \end{cases} \tag{2}$$

2.1 Definition of the ejecta size range

The ejecta size range was defined using the work of Latino *et al.* [8, 14] as a reference. For higher values of β, L_2 moves towards the smallest primary, whereas L_1 and L_3 approach the Sun [8, 14]. Therefore, the proposed mission relies on halo orbits around the second Lagrangian point, which is the most suitable owing to its proximity to the asteroid. Moreover, this behavior implies that the effects linked to J_2 are more pronounced at L_2 than at L_1. L_2, in fact, moving closer to Ryugu for a higher β, will experience an increasing J_2 perturbation. However, the shifts in the positions of the libration points owing to J_2 are on the order of centimeters and can therefore be neglected, as proposed in Refs. [8, 14].

The size range of the particles of interest for the proposed mission can be defined using similar reasoning. In fact, if L_2 gets closer to Ryugu at higher β, which implies smaller particles, then a lower limit must be imposed on the particle sizes to provide a closed region to the ejecta around the asteroid for their free movement. Following Refs. [8] and [14], a distance of 3 km from Ryugu was fixed. In these studies, the range of 3 km was determined by imposing a size range of interest. In our study, the same value was chosen to perform a valid comparison of our approach with the existing approaches. However, further studies and parametric analyses for different distances should be conducted.

For this distance, we obtained $\beta = 8.02315 \times 10^{-4}$. By using this value as well as the following:

- $c_R = 0.07$ [7] (not assuming ideal specular reflection, which corresponds to $c_R = 2$, as used in Refs. [14] and [8]), and
- ejecta density, $\rho_p = 1282$ kg/m^3 (by approximating the ejecta density to be the same as the bulk density of Ryugu, i.e., $\rho_p = 1282$ kg/m^3 (see Table 1))

in Eq. (1), the particle size corresponding to this scenario was found to be $r_P \approx 78.5$ μm.

Because there is no physical upper constraint on the particle dimensions, a maximum size for the asteroid ejecta equal to $r_P = 10$ mm, i.e., $\beta = 6.29804 \times 10^{-6}$, was imposed. For these limiting cases, as shown in Figs. 1 and 2, the particle dimensions are restricted to the range of $78.5\,\mu\text{m} \leqslant r_P \leqslant 10\,\text{mm}$.

3 Database creation

Having defined the size range of interest, the next step was to build a database for characterizing the ejecta dynamics, which could store the ejection and impact parameters, the time of flight, and the final fate of that sample trajectory. Such a database not only allows the easy management of the recovered information but also enables searching for specific initial conditions and directly recovering the final state. The parameters included in the database are:

- r_P, the particle's dimension;
- θ and θ_{imp}, which are respectively the longitude of ejection and that of the impact on the asteroid, if any;
- v_{ej} and v_{imp}, which are respectively the modules of the ejecta's speed at ejection and that at the impact on the asteroid, if any. Both are expressed with respect to the asteroid's velocity in the cartesian synodic frame.
- γ and γ_{imp}, where γ is the ejection angle, which is the angle between v_{ej} and the local normal to Ryugu's surface when the particle is leaving the asteroid, and γ_{imp} is the angle between v_{imp} and the local normal at the location of the particle's impact on the asteroid. An illustration is shown in Fig. 3.
- tof, the time of flight for the sample trajectory, from ejection/rebound to impact/escape.
- Condition, which is a string identifying the final fate of the ejecta.

The database's structure is shown in Appendix B.

The database was used to identify the sample trajectories that fell within one of the following categories:

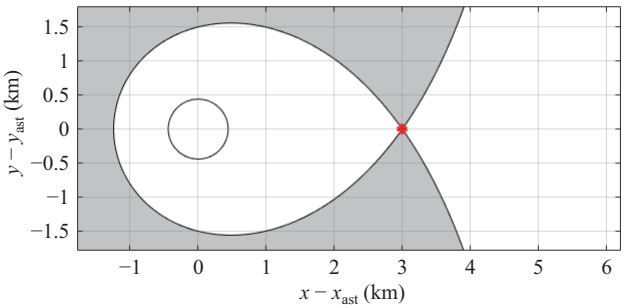

Fig. 1 Zero velocity curve obtained for $r_P \approx 78.5$ μm, corresponding to a lightness parameter $\beta = 8.02315 \times 10^{-4}$. In this scenario, the libration point is localised at 3 km from Ryugu's surface.

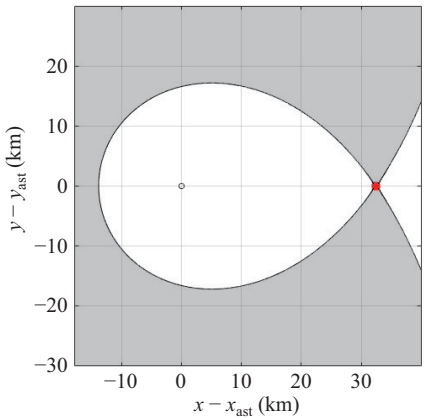

Fig. 2 Zero velocity curve obtained for $r_P = 10$ mm, corresponding to a lightness parameter $\beta = 6.29804 \times 10^{-6}$. In this scenario, the libration point is localised at 32.48 km from Ryugu's surface.

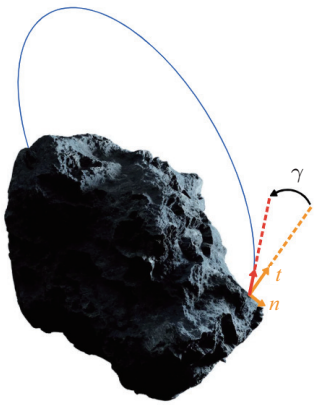

Fig. 3 Image clarifying the definition of γ. The t and n axis are the tangential and normal axis, respectively. The third arrow represents v_{ej}.

(1) particles that re-impact the asteroid shortly after their ejection;

(2) particles that continue to orbit around the asteroid after an imposed time window;

(3) particles that can escape from the system through the bottleneck opened at L_2 (as considered in Refs. [8] and [17]).

Only ejecta of the third class are considered collectible from a satellite orbiting a halo. A detailed outline of the "Condition" entry in the database will be presented in Section 3.3.

3.1 Ejection velocity

To calculate the trajectories, the magnitude of the particle ejection velocity must first be calculated. Specifically, owing to the presence of an integral of motion (i.e., the Jacobi constant), if the position and energy level are fixed, the velocity can be unequivocally determined [8, 14]. This allows using the energy to determine the velocity by computing the magnitude of the ejecta velocity with respect to the prescribed energy level. For this purpose, the selected reference level corresponds to the second Lagrangian point, named C_2, because it represents the threshold value required to open a bottleneck in the zero velocity curves (ZVCs) and escape from the system [17]. Therefore, the velocity can be expressed as shown in Eq. (3).

$$v_{\mathrm{ej}}(x, y, \beta) = \sqrt{C(x, y, \beta) - C_2} \tag{3}$$

where C is the Jacobian constant (energy level) of the ejecta. The position, that is, the x and y coordinates, depends on the longitude θ, whereas β is directly related to the particle size (see Eq. (1)). The procedure for determining v_{ej} is as follows:

(1) a loop on the particle size, r_{P}, is initialized;
(2) for each value of r_{P}, the β parameter is computed;
(3) from β, the analytical position of L_2 is recovered as calculated in Refs. [8, 14]:

$$x_{\mathrm{L2}} = 1 - \mu + \sqrt{\frac{\mu/(1-\mu)}{\beta}}$$

(4) the L_2 position is used as a guess to numerically solve Eq. (4), which provides the correct coordinates of L_2, as proposed in Ref. [17]. In Eq. (4), γ_2 is the L_2-asteroid distance, and is used to compute C_2;

$$\gamma_2^5 + (3-\mu)\gamma^4 + (3-2\mu)\gamma^3 - \mu\gamma^2 - 2\mu\gamma - \mu = 0 \tag{4}$$

(5) a loop on the longitude θ is initialized;
(6) for each value of θ the following are computed:

$$\begin{cases} x = r\cos\theta \\ y = r\sin\theta \end{cases}$$

with r being the adimensional radius of Ryugu. x, y, and β are used to find $C = -2U(x, y, \beta)$, where U is the gravitational potential of the CR3BP;
(7) v_{ej} is calculated according to Eq. (3).

The two nested cycles scan all possible $r_{\mathrm{P}} - \theta$ combinations, where 78.5 μm $\leqslant r_{\mathrm{P}} \leqslant$ 10 mm and $0° \leqslant \theta \leqslant 360°$. The contour of the results is shown in Fig. 4, where the colorbar shows the ejection velocity v_{ej} expressed in cm/s.

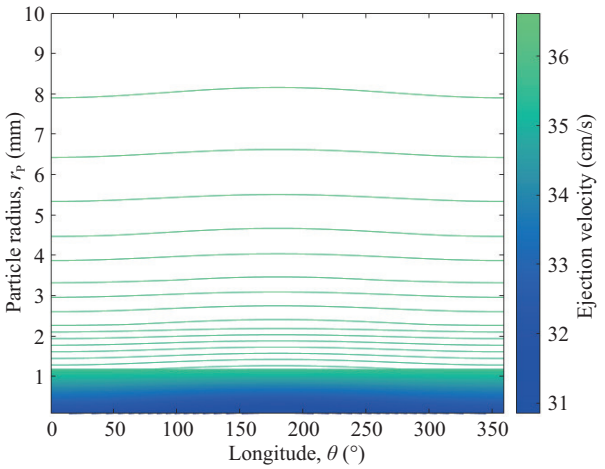

Fig. 4 Contour plot of the particles' ejection velocity v_{ej} as function of their size r_{P} and ejection site longitude θ, for fixed energy level $C = C_2$.

However, Eq. (3) does not consider the rotational contribution of an asteroid. From the normalization of the CR3BP, let ω_{rot} be the rotational velocity of Ryugu around its z-axis and ω_{rev} be the revolutionary velocity of Ryugu. Then, the velocity expression is transformed into [8, 14]:

$$v_0^2 = v_{\mathrm{ej}}^2 + \|\boldsymbol{\Omega} \times \boldsymbol{r}\| = v_{\mathrm{rad}}^2 + \left(\frac{\omega_{\mathrm{rot}}}{\omega_{\mathrm{rev}}} r\right)^2 \tag{5}$$

where $\boldsymbol{\Omega}$ is the vector $[0 \quad 0 \quad \omega_{\mathrm{rot}}/\omega_{\mathrm{rev}}]$, and $\boldsymbol{r} = [r\cos\theta \quad r\sin\theta \quad 0]$. Notably, Eq. (5) relates velocities expressed in adimensional terms.

Equation (3) therefore becomes

$$v_{\mathrm{ej}}^2 + \left(\frac{\omega_{\mathrm{rot}}}{\omega_{\mathrm{rev}}} r\right)^2 = C(x, y, \beta) - C_2$$

$$\Longrightarrow v_{\mathrm{ej}} = \sqrt{C(x, y, \beta) - \left(\frac{\omega_{\mathrm{rot}}}{\omega_{\mathrm{rev}}} r\right)^2 - C_2} \tag{6}$$

Therefore, the velocity will no longer be perfectly radial because the asteroid's rotation will deflect its direction from the already introduced angle γ. Thus, the initial velocity in the cartesian frame can be calculated using

Eq. (7):

$$\boldsymbol{v}_0 = \begin{bmatrix} v_\gamma \cos(\gamma+\theta) - v_\omega \sin\theta \\ v_\gamma \sin(\gamma+\theta) + v_\omega \cos\theta \\ 0 \end{bmatrix} \tag{7}$$

with

$$\begin{cases} v_\omega = \dfrac{\omega_{\text{rot}}}{\omega_{\text{rev}}} r \\ v_\gamma = -v_w \sin\gamma + \sqrt{v_\omega^2 \sin^2\gamma + v_{\text{ej}}^2} \end{cases} \tag{8}$$

This procedure allows for the addition of the contribution of the asteroid's rotation to v_{ej}, as shown in Fig. 4. Thus, by discretizing γ, we can retrieve the initial conditions for the time integration.

In particular, numerical propagation is stopped whenever any one of the following eventsrelated to the ejecta distance from the asteroid, r_{dist}, is observed:

(1) $r_{\text{dist}} \geqslant r_{\text{Hill}} = (\mu/3)^{1/3}$, where r_{Hill} is the radius of the Hill's sphere, which is the region where the gravitational fields of the primaries have a comparable effect on the particles' motion [17, 18]. When this event is detected, the integration is stopped since the particle is considered to have successfully left Ryugu's system through the bottleneck at L_2.

(2) $r_{\text{dist}} \leqslant r_{\text{Ryugu}}$, which is a condition for an impact on the asteroid's surface.

In the second scenario, a collision occurs between the ejecta and Ryugu's surface, indicating that it is necessary to evaluate the bouncing behavior. This is achieved by exploiting the coefficients of restitution.

3.2 Coefficients of restitution for bouncing behavior

The coefficient of restitution, ϵ, is defined as the ratio of the relative velocities of the two colliding bodies before and after impact. However, in this case, one of the bodies is an asteroid, which represents an immovable surface for the particle, leading to

$$\epsilon = \frac{v_{\text{f}}}{v_0} \tag{9}$$

where v_{f} is the particle velocity after impact and v_0 is the velocity immediately before impact. Re-impacts are likely to occur at oblique angles, meaning that two separate coefficients, one for the normal direction and the other for the tangential direction, must be identified. Their expression is given in Eq. (10), where ϵ_{n} and ϵ_{t} represent the normal and tangential restitution coefficients, respectively.

$$\begin{cases} \epsilon_{\text{n}} = \dfrac{v_{\text{nf}}}{v_{\text{n0}}} \\ \epsilon_{\text{t}} = \dfrac{v_{\text{tf}}}{v_{\text{t0}}} \end{cases} \tag{10}$$

In the previous works of Latino *et al.* [8, 14], these coefficients were arbitrarily considered to be constant and assumed to be $\epsilon_{\text{n}} = 0.6$ and $\epsilon_{\text{t}} = 0.74$. This implies that all collisions are treated in the same manner, neglecting the possible differences arising from varying impact angles. To avoid this simplification, a different approach is adopted. In particular, the novel methodology used here is based on the work of Kikuchi *et al.* [9], in which the trends of ϵ_{n} and ϵ_{t} with respect to the impact angle were calculated, considering both a point mass (PM) model and the rigid body (RB) approximation. Furthermore, these trends were observed at two different sites on Ryugu: TDM1 and TDM2. Even though both of these sites are close to the equator, TDM1 and TDM2 are representative, respectively, of the surface and sub-surface materials. However, Figs. 5 and 6 show the behavior of the coefficients for TDM1 and TDM2, respectively.

As shown in Figs. 5 and 6, for both sites, the point mass model allows rebounds for a wider range of impact angles, which directly reflects the more conservative nature of the point mass model [9].

The values shown are discretized on the impact angle α, which was previously called γ_{imp}. The aim here is to correctly compute (within a certain error) the restitution coefficients for each specific impact. For this reason, the work flow proposed here includes an interpolation of the data provided in Ref. [9] using the MATLAB commands *polyfit* and *polyval*. Using the obtained polynomial coefficients, the ϵ_{n} and ϵ_{t} values for the impact angle of any collision can be computed. However, this procedure requires imposing order n_{ord}, which approximates the trend of the function to be interpolated. Thus, to obtain the best possible results, n_{ord} was varied from two to $n_{\max}$, where $n_{\max}$ represents the maximum order suitable for interpolation, beyond which the polynomial results become undetermined or poorly conditioned. In particular, its value depends on the number of nodes, as provided by Kikuchi *et al.* [9]. The trends of the error in ϵ_{n} and ϵ_{t} for both the rigid body and point mass models are shown in Figs. 7 and 8. These show only the case of TDM1; the case of TDM2 has been omitted for brevity. However, the conclusions were the same for both TDMs.

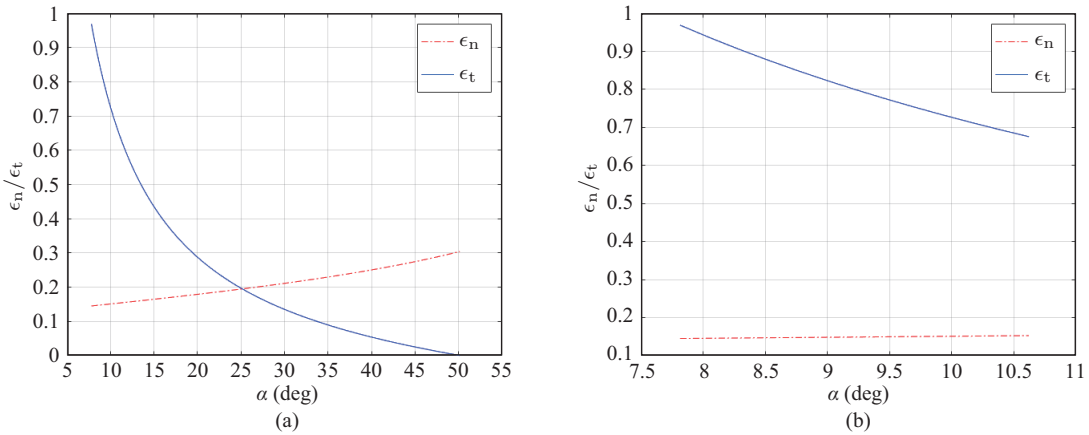

Fig. 5 Restitution coefficients for TDM1, applying the point mass model (a) and the rigid body assumption (b). In both cases, α is the impact angle and ϵ_n and ϵ_t are the normal and tangential restitution coefficients, respectively.

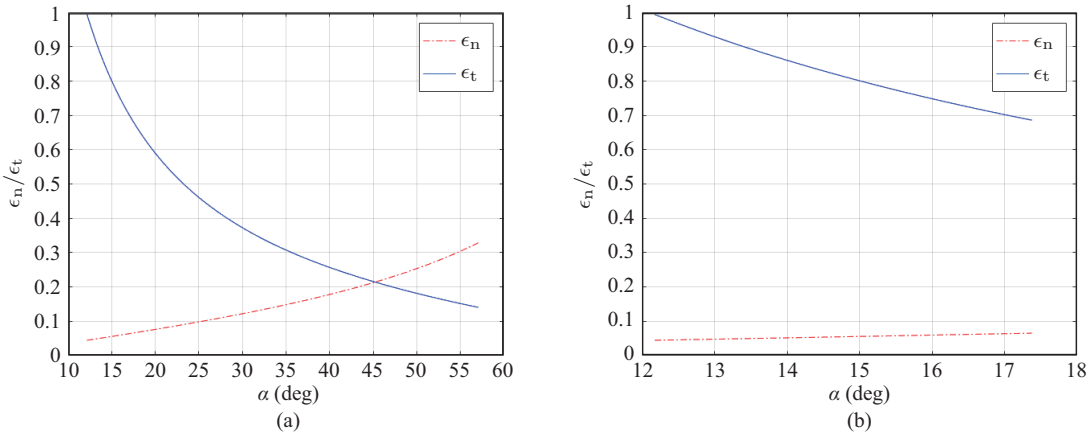

Fig. 6 Restitution coefficients for TDM2, applying the point mass model (a) and the rigid body assumption (b). In both cases, α is the impact angle and ϵ_n and ϵ_t are the normal and restitution coefficients, respectively.

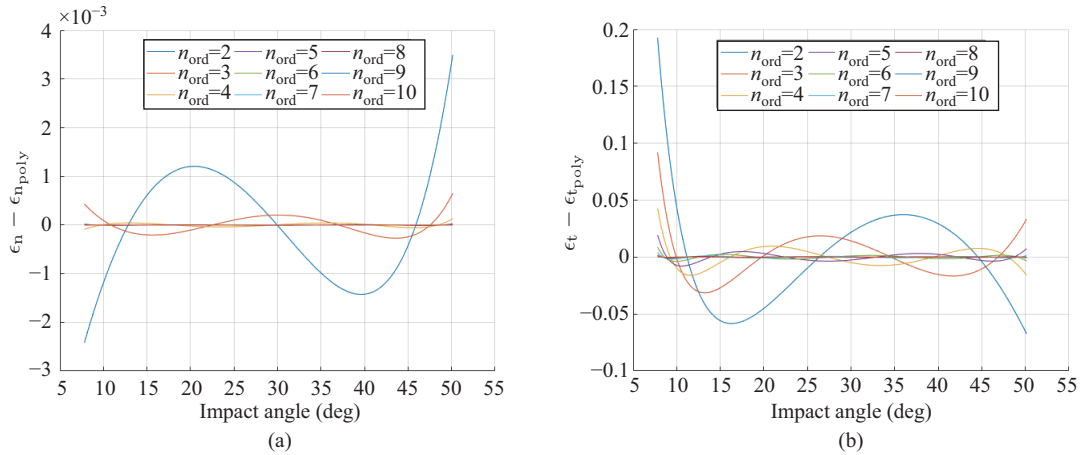

Fig. 7 Interpolation error in estimating ϵ_n (a) and ϵ_t (b) for TDM1-PM depending on the interpolation order n_{ord} applied.

As Figs. 7 and 8 show, the error tends to decrease with increasing values of n_{ord}, as confirmed by the mean squared error (MSE) computed for each interpolation order. In conclusion, the reasoning provides the best orders of interpolation for the available data, as reported in Table 2. The results also show that, in all the cases,

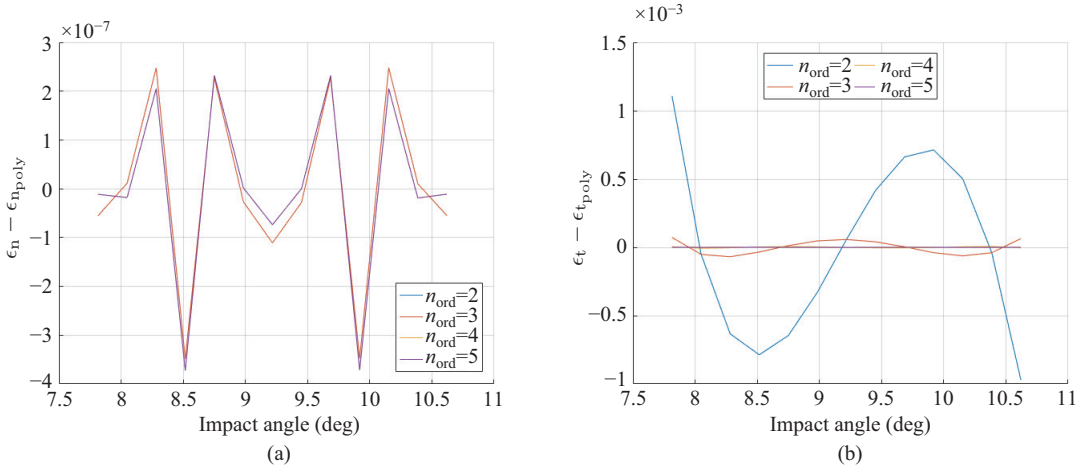

Fig. 8 Interpolation error in estimating ϵ_n (a) and ϵ_t (b) for TDM1-RB depending on the interpolation order n_{ord} applied.

Table 2 Interpolation quality. The first column refers to the TDM considered, the second to the model applied, the third shows the best interpolation order ($n_{ord} = n_{max}$ in all the cases), and the fourth and fifth columns show the mean squared error in ϵ_n and ϵ_t, respectively

TDM	Model	n_{ord}	MSE_{ϵ_n}	MSE_{ϵ_t}
TDM1	PM	10	1.5474×10^{-12}	6.4770×10^{-08}
TDM2	PM	10	4.2685×10^{-12}	5.4987×10^{-09}
TDM1	RB	5	9.5038×10^{-14}	3.2857×10^{-13}
TDM2	RB	5	8.0180×10^{-13}	5.8779×10^{-12}

the approximation for ϵ_t has a greater error than that for ϵ_n. Furthermore, the table shows that the coefficients are better estimated in the rigid body model because of the higher ratio of the amount of data given to the range of suitable impact angles provided.

The coefficients of restitution thus characterized are then entered into the matrix $\boldsymbol{E}$ defined in Eq. (11).

$$\boldsymbol{E} = \begin{bmatrix} \epsilon_t & 0 & 0 \\ 0 & -\epsilon_n & 0 \\ 0 & 0 & -1 \end{bmatrix} \tag{11}$$

Following Ref. [14], $\boldsymbol{E}$ can be used to reproduce the damping during a collision by applying Eq. (12), where $\boldsymbol{v}_{tn}$ represents the pre-impact velocity and $\boldsymbol{v}_{E_{tn}}$ is the speed damped by the collision. For both, the subscript "tn" indicates that the velocities are expressed with respect to the asteroid's surface tangential–normal reference frame.

$$\boldsymbol{v}_{\boldsymbol{E}_{tn}} = \boldsymbol{E}\boldsymbol{v}_{tn} \tag{12}$$

A proper definition of ϵ_t and ϵ_n, allows for a more precise computation of $\boldsymbol{v}_{\boldsymbol{E}_{tn}}$. This is crucial because the bouncing behavior can be investigated by using $\boldsymbol{v}_{\boldsymbol{E}_{tn}}$. First, it is necessary to differentiate between ejecta that bounce back to orbit around the asteroid after colliding with Ryugu's surface and those that start rolling on its soil and, eventually, landing on it. Following Latino [14], a threshold height was fixed to identify this behavior. If a rebounding particle reached altitudes beyond this height, it was considered to bounce rather than roll on Ryugu. By applying the energy balance shown in Eq. (13), the maximum altitude on Ryugu's surface gained by the particle after the collision (i.e., the altitude reached when the energy is completely transformed into potential energy) can be computed by simply determining the post-impact velocity along the normal direction (v_n).

$$\frac{1}{2}v_n^2 = gh \Longrightarrow h = \frac{v_n^2}{2g} \tag{13}$$

The possibilities are as follows:

- $h > l_{threshold}$: the particle goes back into orbit. New ICs are generated, and the propagation continues until the next event or the end of the time window considered.
- $h < l_{threshold}$: the particle lands on the asteroid. The simulation stops, and the next iteration begins.

The value of $l_{threshold}$ should be reasonably low and is set in this case to 10 cm [14]. v_n can be calculated once $\boldsymbol{v}_{\boldsymbol{E}_{tn}}$ is known, allowing the use of Eq. (13). In the case where the particle bounces back into the orbit, the matrix $\boldsymbol{R}$ is defined as follows: The angle ξ between the cartesian and tangential–normal frames' first axes is determined following Ref. [14]. $\boldsymbol{R}$ is constructed as shown in Eq. (14). Using $\boldsymbol{R}$, the damped velocity vector obtained using Eq. (12) can be rotated to the cartesian frame introduced in Eq. (2) according to Eq. (15). To this

value of $\boldsymbol{R}$, the asteroid's rotational contribution must be added following the previous discussion to obtain new initial conditions for the propagation of the post-rebound trajectory.

$$\boldsymbol{R} = \begin{bmatrix} \cos\xi & \sin\xi & 0 \\ -\sin\xi & \cos\xi & 0 \\ 0 & 0 & 1 \end{bmatrix} \tag{14}$$

$$\boldsymbol{v}_{\text{cartesian}} = \boldsymbol{R}^{\mathrm{T}} \boldsymbol{v}_{\boldsymbol{E}_{\text{tn}}} \tag{15}$$

3.3 Comparison with previous studies

The procedure for generating the initial ejection conditions described above is iterated using three nested loops on particle size r_{P}, longitude θ, and ejection angle γ. For clarity, a code block diagram is presented in Appendix A.

As the program runs, the database is filled line-by-line with the parameters introduced at the beginning of Fig. A2. Specifically, the "Condition" column, which returns the final fate of the ejecta, will present one of the following categories:

- Escape: the ejecta particle could escape from the system through the L_2 bottleneck.
- Impact: after orbiting around the asteroid for a timespan equal to tof, the ejecta particle collided with Ryugu's surface with an impact angle within the feasible range.
- OutRange: after orbiting around the asteroid for a timespan equal to tof, the ejecta particle collided with Ryugu's surface with an impact angle outside the feasible range. In this case, the particle is considered to have landed on the surface, unable to bounce back into orbit.
- Orbit: in this case, tof $= t_{\max}$. Therefore, the ejecta has orbited around the asteroid without impacting it again or escaping from the system. In this case, the ejecta is assumed to still be in orbit around Ryugu.
- Escape$_{\text{reb}}$: the ejecta particle could escape from the system through the L_2 bottleneck after a collision with Ryugu and consequent rebound.
- Impact$_{\text{reb}}$: after a collision with Ryugu and the consequent rebound, the particle orbits around the asteroid for a timespan equal to tof before colliding again with Ryugu's surface with an impact angle within the feasible range.
- OutRange$_{\text{reb}}$: after a collision with Ryugu and the consequent rebound, the particle has been orbiting around the asteroid for a timespan equal to tof before colliding again with Ryugu's surface with an impact angle outside the feasible range.
- Orbit$_{\text{reb}}$: after a collision with Ryugu and the consequent rebound, the ejecta has orbited for tof $= t_{\max}$ without impacting again on the asteroid's surface or escaping from the system. In this case as well, the ejecta is assumed to still be in orbit around Ryugu.

The maximum time span imposed was $t_{\max} = 90$ days, which is considered to be sufficiently large with respect to the dynamic time scale. Yu *et al.* [18] and Soldini and Tsuda [10] observed that, generally, the generated ejecta plume is cleared after approximately two weeks.

According to the discussion in Section 2.1, the particle size varied from 78.5 μm to 10 mm. Moreover, following Trisolini *et al.* [6, 19], γ was considered to range from $-65°$ to $-25°$ and from $25°$ to $65°$. Finally, θ was discretized once per degree from $0°$ to $360°$.

The differences arising from applying the new approach described above to recover the coefficients of restitution were investigated. Figure 9 presents a global view of the sample trajectory distribution, considering the different categories introduced above. For brevity, this is only shown for TDM1 and PM.

Notably, because no limits were imposed in Ref. [14] on the impact angle suitable for rebound, when studying the dynamics using the approach of Latino, the categories OutRange and OutRange$_{\text{reb}}$ will be empty. Another important difference is in the number of rebounds. Using the coefficients reported in Ref. [14], the sample trajectories arising from a rebound were found to be 522,349, which is considerably higher than the 131,853 obtained by interpolating the data, as proposed in this study. This trend is a direct consequence of the fact that Latino [14] considered that any particle can possibly rebound independently of the impact angle. Furthermore, the restitution coefficients used by Latino [14], especially those for ϵ_{n}, are higher than those obtained for the PM case shown in Fig. 5. This results in lower energy dissipation during a collision, which causes more particles to have enough velocity to bounce off from Ryugu after the impact. As shown in the figure, almost all the impact trajectories are followed by a successful rebound. Moreover, the three populated categories shown in blue have comparable numbers of samples, which implies that a large number of the trajectories falling into the Impact$_{\text{reb}}$ category lead to a particle being injected into the orbit around Ryugu after a second

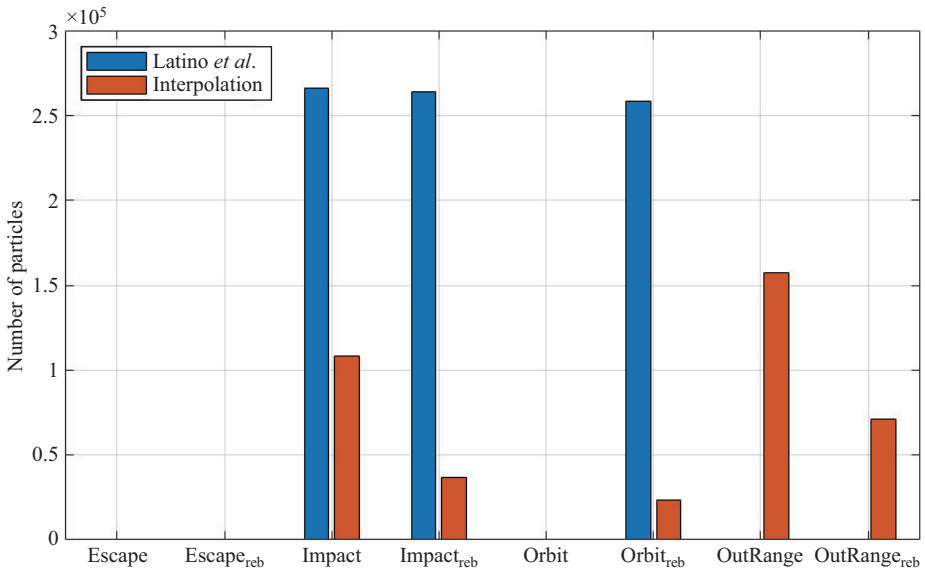

Fig. 9 Comparison between the sample trajectories' fate calculated using the coefficients of restitution used by Latino [14] and those obtained through interpolation, for PM-TDM1.

rebound. More precisely, of the 263,728 trajectories in the $\text{Impact}_{\text{reb}}$ category, approximately 98% result in the particle entering the orbit after a second rebound. This means that the studies by Latino [14] and Ref. [8], prior to the mission itself, did not return realistic trends, highlighting the importance of in-loco data acquisition. The results of these analyses demonstrate the importance of considering more accurate data to predict the behavior of the generated ejecta. However, the results also show that these post-rebound orbits can hardly provide suitable conditions for an in-orbit collection scenario, such as the one analyzed in this work. In fact, Fig. 9 shows that no particles escaped from the system, suggesting that the collection strategy in the proposed mission is infeasible. This is a consequence of considering only the position of the lagrangian point. In an improved model, the region of interest should be expanded to include the halo region around the libration point.

This implies changing the reference energy level referring v_{ej} no longer to C_2 but to $C' < C_2$. Thus, the analysis of periodic orbits in the neck region is crucial for the development of an improved model and is discussed in Section 4.

4 Neck region trajectory

In this section, we discuss particle motion in the neck region, that is, the motion connecting the inner and outer allowed realms. Following Ref. [17], the linearized lagrangian equations of motion can be expressed as Eq. (16), which can also be written in the vector matrix form shown in Eq. (17).

$$\begin{cases} \dot{x} = v_x \\ \dot{y} = v_y \\ \ddot{x} = \dot{v}_x = 2v_y + ax \\ \ddot{y} = \dot{v}_y = -2v_x - by \end{cases} \tag{16}$$

$$\begin{bmatrix} \dot{x} \\ \dot{y} \\ \dot{v}_x \\ \dot{v}_y \end{bmatrix} = \begin{bmatrix} 0 & 0 & 1 & 0 \\ 0 & 0 & 0 & 1 \\ a & 0 & 0 & 2 \\ 0 & -b & -2 & 0 \end{bmatrix} \begin{bmatrix} x \\ y \\ v_x \\ v_y \end{bmatrix} \tag{17}$$

Let the matrix on the right-hand side of Eq. (17) be $\boldsymbol{M}$. The matrix $\boldsymbol{M}$ has two real and two imaginary eigenvalues, $\pm\lambda$ and $\pm \mathrm{i}\nu$, respectively, corresponding to the eigenvectors $\boldsymbol{u}_1, \boldsymbol{u}_2, \boldsymbol{\omega}_1, \boldsymbol{\omega}_2$. The general solution of Eq. (17) has the form shown in Eq. (18), where α_1, α_2 are real, and $\beta = \alpha_1^2 + \mathrm{i}\alpha_2^2$ is complex.

$$\boldsymbol{x} = (x, y, \dot{x}, \dot{y}) = \alpha_1 \mathrm{e}^{\lambda t} u_1 + \alpha_2 \mathrm{e}^{-\lambda t} u_2 + 2\,\mathrm{Re}(\beta \mathrm{e}^{\mathrm{i}\nu t} \omega_1) \tag{18}$$

This solution is strongly dependent on α_i. In fact, following Koon *et al.* [17], nine different classes of orbits can be distinguished for different combinations of the signs of α_i. The Lyapunov orbit that arises for $\alpha_1 = \alpha_2 = 0$ is particularly relevant to this work. According to Conley [20], this periodic orbit projects onto the xy-plane as an ellipse centered at L_2, with the lengths of

its major and minor axes equal to $2\tau\sqrt{\chi/k}$ and $2\sqrt{\chi/k}$, respectively. Although χ is a variable that determines the amplitude of the orbit, k is a constant that can be computed as Eq. (19):

$$k = -a + b\tau^2 + \nu^2 + \nu^2\tau^2 \quad \text{with } \tau = -\left(\frac{\nu^2 + a}{2\nu}\right) \tag{19}$$

To extend the region of interest to a halo neighborhood, the energy levels corresponding to the ZVCs should be decreased. In particular, instead of the energy level C_2, one with a slightly higher energy, called $C' = 0.9999999999997C_2$ (C_2 is negative), should be considered. This value not only highlights how sensitive to the energy levels this problem is, but this sensitivity also manifests in how the ZVCs are affected by it. The new ZVCs, shown in Fig. 10 for both $r_P = 78.5$ μm and $r_P = 10$ mm, still present a shape that provides important hints regarding the direction from which the particles escape. To explain this concept, Fig. 11 shows the ZVC for $C'' = 0.999999999999C_2$, which highlights that, for a small change in energy, the accessible realm becomes too wide to provide a functional indication of where the particles escape from the system.

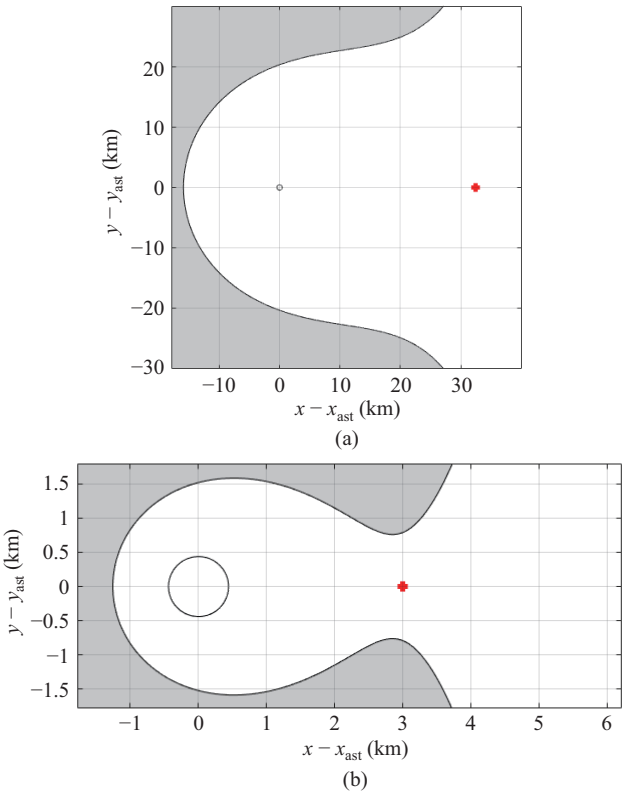

Fig. 10 Zero velocity curve for energy level fixed at C' for $r_P = 10$ mm (a) and $r_P = 78.5$ μm (b).

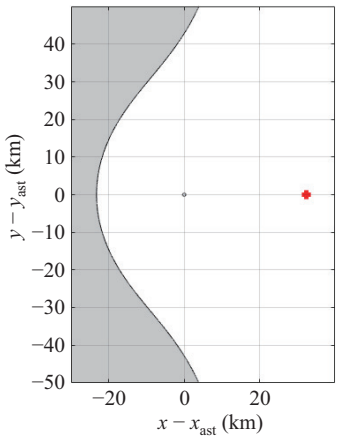

Fig. 11 Zero velocity curve for energy level fixed at C'' for $r_P = 10$ mm.

Assuming that the new energy level C' is of interest, the motion of particles can be designed to be within the region corresponding to the bottleneck. This was done, through Eq. (20), for both values of r_P to understand the advantages or drawbacks arising from the different values of r_P. Specifically, for $r_P = 78.5$ μm and $r_P = 10$ mm, a semi-major axis (SMA) of 0.75 and 28.5 km was considered to lead to orbits with high coverage of the bottleneck. The adimensional values of χ can be calculated using Eq. (20). These are listed in Table 3.

$$\chi = \left(\frac{\text{SMA}_{\text{adim}}}{\tau}\right)^2 k \quad \text{with } \text{SMA}_{\text{adim}} = \frac{\text{SMA}}{l_{\text{ref}}} \tag{20}$$

Table 3 ϵ values for cases with $r_P = 78.5$ μm and $r_P = 10$ mm

	$r_P = 78.5$ μm	$r_P = 10$ mm
χ	1.6902×10^{-12}	1.9452×10^{-12}

The resulting orbits are shown in Fig. 12.

In the case of $r_P = 78.5$ μm, the small dimension of the obtained orbit enables the spacecraft to quickly "survey" the region of the entire opened bottleneck. Therefore, in this scenario, almost all the ejecta escaping from the bottleneck with sizes close to 78.5 μm can be assumed to be captured. However, the largest particles cannot pass through the same aperture; therefore, only a small portion of this type of ejecta can be considered to have been collected. However, a larger orbit, such as that obtained for $r_P = 10$ mm, enables the capture of particles with a wider range of sizes. In fact, the majority of ejecta escaping from the system passes through the portion of space covered by the orbit. However, because the orbit

is considerably larger, it cannot be ensured that when an ejecta escapes, the spacecraft will be in the vicinity to capture it and not in another tract of its path. This problem can be partially overcome by placing two capture spacecraft at the two ends of the orbit to increase the capture probability. However, such a strategy would have a heavy impact on mission costs, and studies on spacecraft coordination would be required. Nevertheless, it could increase the mission's reliability and guarantee operations despite the loss of one satellite. These aspects are left for future research.

Therefore, the reference solution is chosen first, as it enables the maximization of the capture probability. However, choosing this option does not mean that only particles with $r_{\mathrm{P}} = 78.5$ μm will be captured, as all the particles, irrespective of their size, can pass through that region of space. Nevertheless, this choice favors the collection of smaller particles. With this choice, the number of particles smaller than $r_{\mathrm{P}} = 78.5$ μm that escaped was zero, but collection of particles with sizes $r_{\mathrm{P}} = 1.181$ mm and $r_{\mathrm{P}} = 2.283$ mm is enough to consider the capture satisfactory.

5 Simulation results

First, the number of particles in each category was determined, as shown in Figs. 13 and 14 for the point-mass and rigid-body models, respectively. The rigid-body model used in the simulations was that developed by Kikuchi *et al.* [9], in which both the asteroid's soil and

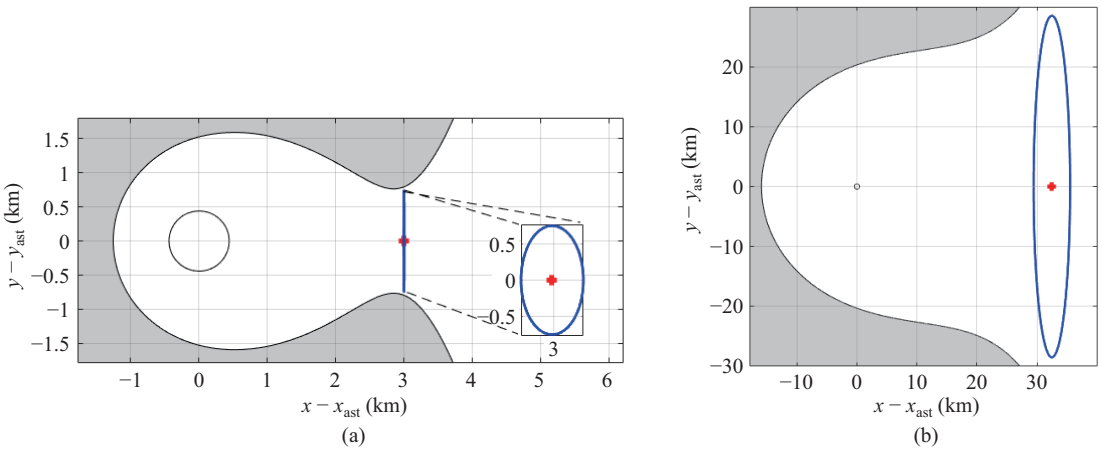

Fig. 12 Periodic orbit in the neck region formed by the ZVC with $C = C'$ for $r_{\mathrm{P}} = 78.5$ μm (a) and $r_{\mathrm{P}} = 10$ mm (b).

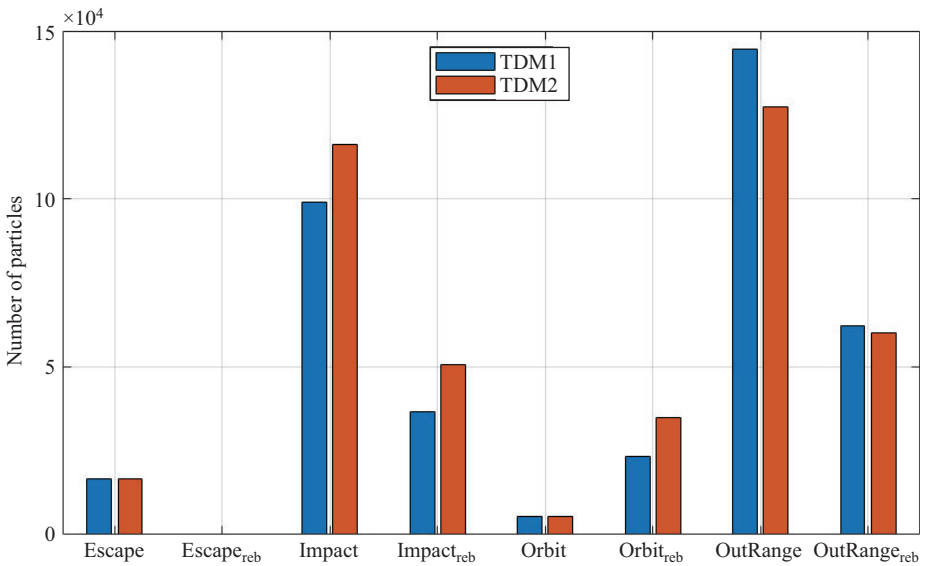

Fig. 13 Histogram of the number of ejecta falling within each category in the point mass model.

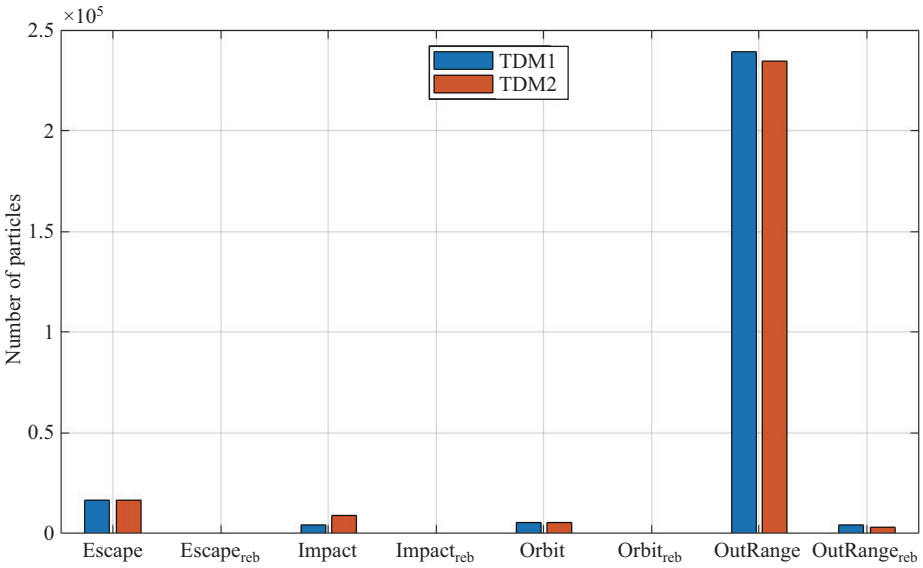

Fig. 14 Histogram of the number of ejecta falling within each category in the rigid body model.

ejecta are modeled as rigid surfaces/spheres. Although reasonable for a first-step analysis, this model neglects the tangential compliance caused by elastic deformation, which affects the tangential impulse. Although such an effect is expected to be negligible for low-velocity impacts, it may be a subject of interest for future research.

As shown in the figures, the number of particles escaping the system remains the same in both the PM and RB approximations, equal to 16,610 for both TDM1 and TDM2. This can be explained by recalling the difference between PM and RB models, which is the range of suitable impact angles. Therefore, either approach will not affect the behavior of particles that do not impact Ryugu, or the *Escape* or *Orbit* categories, which account for 5588 ejecta. Nevertheless, although these numbers remain the same, the corresponding percentages change, as highlighted in Table 4. However, changing the model will result in a drastic change in the number of ejecta categorized as *OutRange*. Finally, in all the cases, for the category $\text{Escape}_{\text{reb}}$, no particle could escape from the system after a previous rebound. A simple reason is that if a particle is ejected with conditions that do not permit a direct escape, that particle will never be able to leave the system even after a "re-tuning" of its initial conditions by means of an impact at Ryugu. This is a consequence of the energy dissipation occurring in any collision.

Table 4 Percentages of ejecta falling in each category with respect to the total trajectories computed for each scenario

(Unit: %)

	TDM1		TDM2	
	PM	RB	PM	RB
Escape	4.2820	6.1476	4.0390	6.1717
Impact	25.5078	1.6058	28.2682	3.3291
Orbit	1.4408	2.0686	1.3591	2.0767
OutRange	27.2735	88.5271	30.9506	87.1572
$\text{Escape}_{\text{reb}}$	0	0	0	0
$\text{Impact}_{\text{reb}}$	9.4676	0.0470	12.3214	0.03939
$\text{Orbit}_{\text{reb}}$	5.9877	0.0448	8.4655	0
$\text{OutRange}_{\text{reb}}$	16.0400	1.5588	14.5960	1.2256

However, because the differences between TDM1 and TDM2 are minimal, only the results for the TDM1 case will be shown here because of its representation of the surface material, which is of interest in this work. Furthermore, owing to its more conservative formulation, we will use the PM model, even though the RB model represents a better approximation of the real scenario.

In addition, we assume that there is no mutual interaction among the particles in the ejecta plume because all the ejecta will be generated from the same initial plume, meaning that once the remaining particles start orbiting for some revolutions, the smaller particles will have already left the neighborhood of the asteroid. Therefore, interparticle interactions can be safely neglected.

We focus only on the escaped ejecta, as the feasibility of the mission is largely determined by them. Figures 15 and 16 show two contour plots depicting the trajectories

of the escaping particles with respect to r_P, θ, and γ_{ej}.

Figure 15 shows that the conditions under which a particle can escape can be divided into two groups: one in which $\theta < 100°$ and the other in which $200° < \theta < 350°$. Moreover, a higher r_P leads to a wider suitable θ range, thereby allowing more particles to escape. As shown in the figure, most of the ejecta leaving Ryugu belong to the first group, while no particles were found to escape

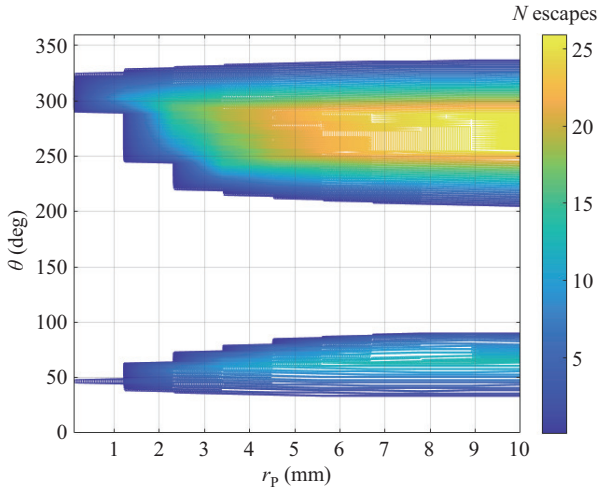

Fig. 15 Contour plot of the trajectories of the samples that escaped the neighborhood of the asteroid as function of r_P and θ for PM-TDM1. Colorbar shows the number of particles that escaped successfully. A larger number of particles was found to escape in the range of $200° < \theta < 350°$, and the number increased with particle size.

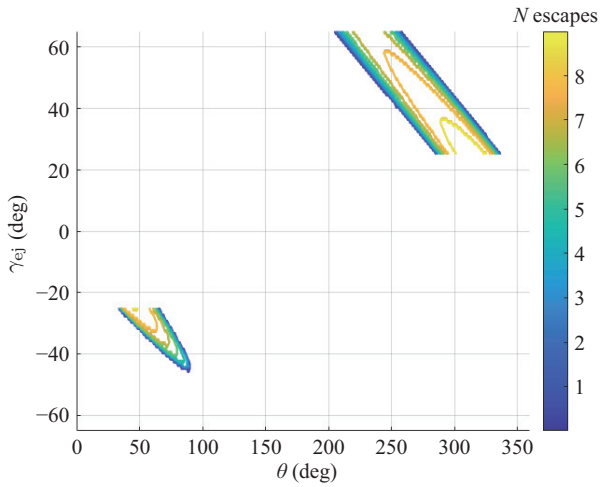

Fig. 16 Contour plot of the trajectories of the samples that escaped the neighborhood of the asteroid as function of θ and γ_{ej} for PM-TDM1. Colorbar shows the number of particles that escaped successfully. The number of particles that escaped at lower θ decreases as the longitude increases, the number of particles that escaped at higher θ show the opposite trend.

when $100° < \theta < 200°$. Figure 16 shows that for the first group, for most of the particles with escaping orbits, the θ values were the lowest and the γ_{ej} values were the highest. As θ increased, the number of escaped particles decreased and required lower γ_{ej} values. By contrast, the other group exhibited the opposite trend: the number of particles that escaped was higher for lower values of γ_{ej} and increased with θ. This is a consequence of the geometry of the problem and constitutes the condition that maximizes the escape probability of a particle to be ejected directly towards the bottleneck.

The other crucial parameter to assess the feasibility of the collection strategy is the time window required by the mission. Specifically, the parameter that can distinguish between failed and successful missions is the collected mass. By choosing the mass collected by the Hayabusa2 mission, i.e., about 5.262 g [21], as the threshold value for the gathered mass, the time required by the collection mission can be estimated. This value was considered suitable for a preliminary feasibility assessment of the mission for the in-orbit collection of samples generated by small kinetic impactors. By sorting the escaped ejecta by size (see Fig. 17) and approximating the particle density by the bulk density (see Table 1), the escaped mass for each particle size can be calculated. This is illustrated in Fig. 18. For $r_P \approx 1.181$ mm and $r_P \approx 2.283$ mm, the collected masses were 1.804 and 60.343 g, respectively, and no particles were found to escape for $r_P = 78.5$ μm.

Let us consider the case of a satellite orbiting the left trajectory shown in Fig. 12. By maximizing the capture probability, mass equal to the mass threshold can be gathered by simply limiting the r_P value to less than or equal to 2.283 mm. Because a larger r_P corresponds to slower dynamics [7, 16], a large time scale is necessary to collect the mass corresponding to $r_P = 2.283$ mm. By approximating the ejection time as the time the particle takes to leave Hill's sphere, the amount of mass that escaped (and was thus possibly collected) with $r_P = 2.283$ mm is shown in Fig. 19 with respect to time. Through this approach, the time required to collect the requisite 3.484 g (i.e., 5.262–1.804 g) from the ejecta with $r_P = 2.283$ mm was found to be 22.48 days.

It is interesting to estimate the velocity at which the collection will occur. This is fundamental information necessary for the preliminary design of the capture mechanism. In this study, this value is assumed to be the velocity at which the particle leaves Hill's sphere, that

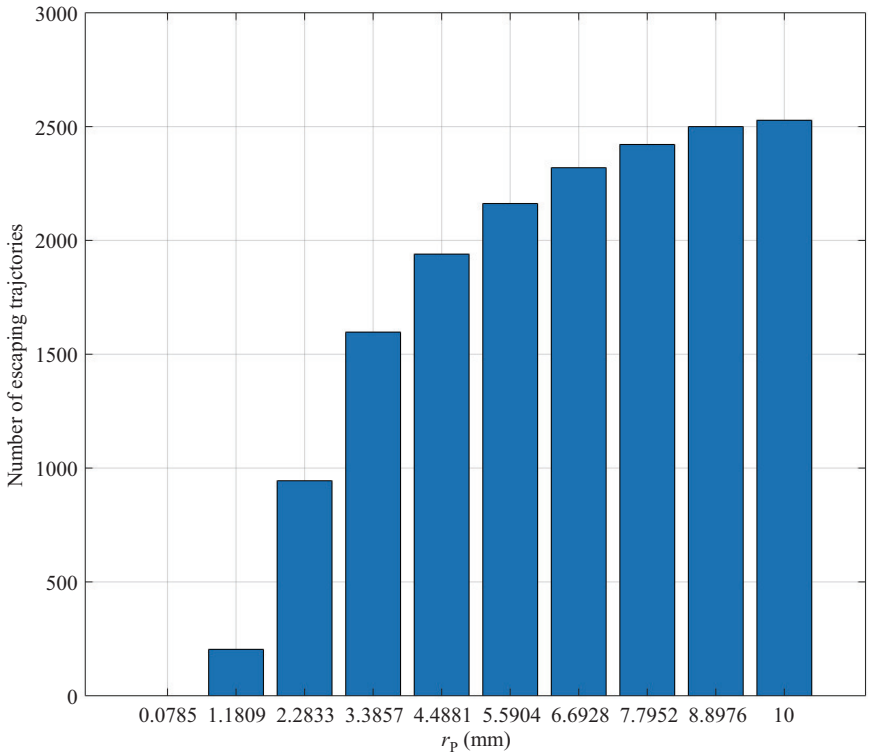

Fig. 17 Number of particles found to escape sorted by the particle size, for PM-TDM1.

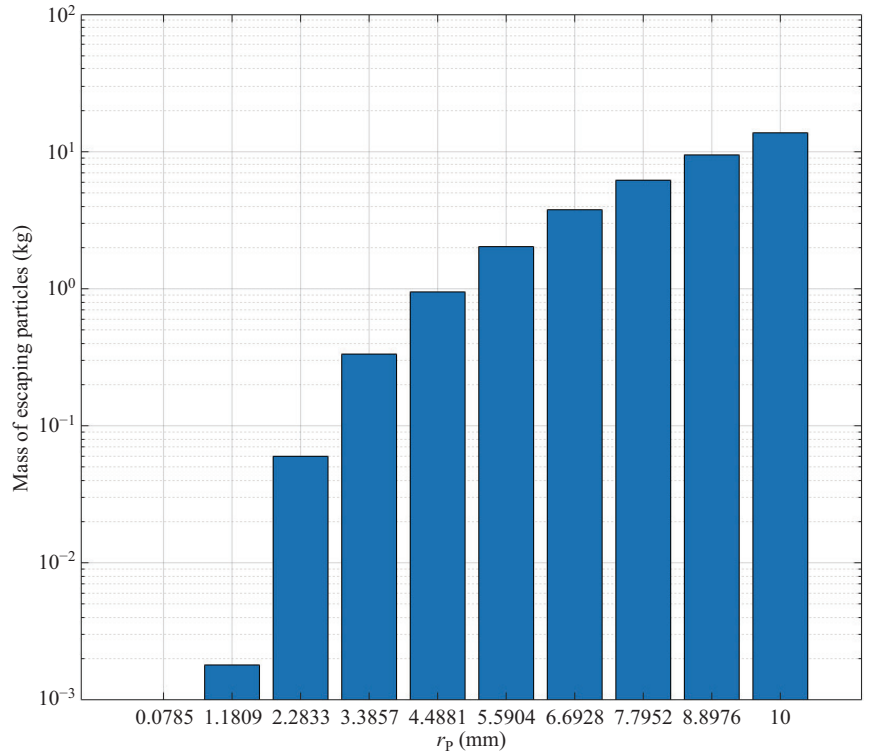

Fig. 18 Bar-graph of the amount of mass found to escape sort by the particle size, for PM-TDM1. Note that the y-axis is in logarithmic scale.

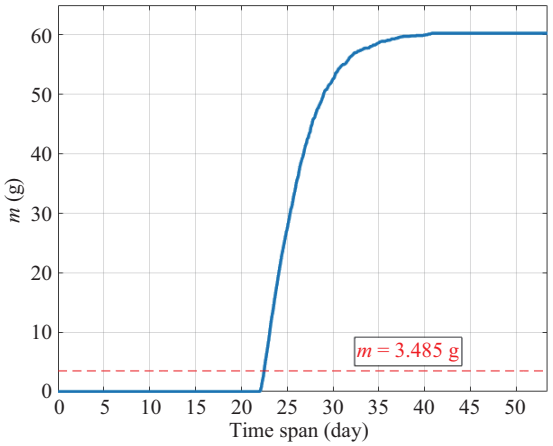

Fig. 19 Collected mass of particles with $r_P = 2.283$ mm over time. The dotted red line represents the threshold mass value of particles with $r_P = 2.283$ mm that the mission should collect to be considered successful.

is, when it is assumed to have successfully escaped. The hypothesis behind this is that the ejecta are captured the moment they exit Hill's sphere. In addition to this, the velocity that should be considered for the capture design is the relative speed between the ejecta and the spacecraft. However, for the preliminary design, the previously explained assumption was retained and applied. Following this idea, the capture velocity is easily calculated by using the conditions required for the "Escape" outcome for $t = \text{tof}$, retrieved from the database. The results are presented in Fig. 20.

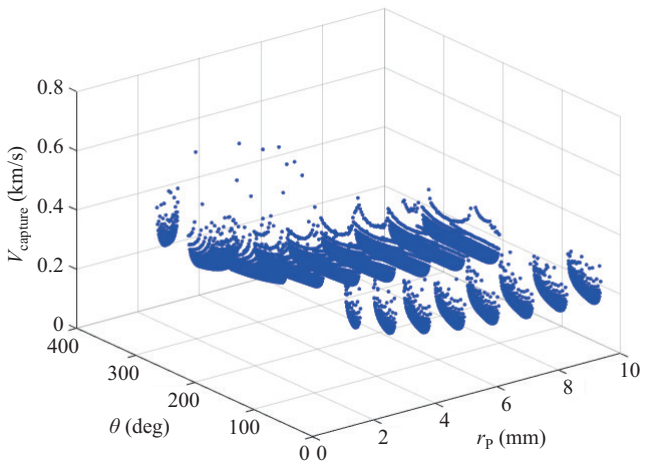

Fig. 20 Capture velocity V_{capture} expressed as a function of r_P and θ, for PM-TDM1. V_{capture} is approximated by the particle's velocity when exiting the system from the L_2 bottleneck.

As shown in the figure, the smaller the ejecta, the higher the capture velocity. This is a positive aspect because otherwise, the kinetic energy of the ejecta at capture would grow with both r_P and V_{capture}, likely reaching prohibitive values. Moreover, this explains why, for the ejecta belonging to the upper group defined in Fig. 15, the capture velocity is slightly smaller on average relative to that of the ejecta in the second group. Figure 15 shows that the largest component of the ejecta is from the first group and that the majority of the ejecta is captured at lower velocities, especially for high r_P. In addition, Fig. 4 shows that larger particles exhibit a higher v_{ej}, which means that, contrary to expectations, particles departing from Ryugu with the highest velocities are the same as those that could be collected, on average, at a lower capture speed, and that the larger the ejecta dimension, the lower the minimum capture speed. In conclusion, this plot also shows that, apart from some isolated cases, almost all particles arrive at a velocity between 100 and 300 m/s. Therefore, estimating the kinetic energy of the particle at which it is captured is important, as the collection mechanism must be designed to effectively dissipate it. The kinetic energy can be easily computed from the value of V_{capture}, and the results are shown as a function of V_{capture} and r_P in Fig. 21.

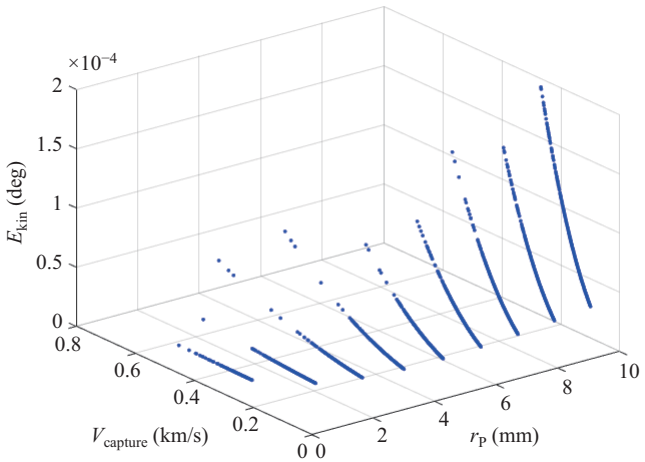

Fig. 21 Kinetic energy E_{kin} of the ejecta at capture as function of r_P and V_{capture}, for PM-TDM1. E_{kin} is approximated by the particle's energy when exiting the system from the L_2 bottleneck.

The graph clearly highlights that the larger particles have a higher kinetic energy even when they present a lower capture velocity. The maximum kinetic energy corresponded to $E_{\text{max}} = 1.9258 \times 10^{-4}$ J. This result is important, because it represents the maximum energy that should be dissipated by the collection mechanism.

This value is used in the preliminary design of the collection technique (see Section 6).

6 Preliminary collection mechanism analysis

This section presents a preliminary analysis of the design of an in-orbit particle collector. Based on the history of debris removal around the Earth, the main components considered for the collection mechanism design were flexible tether nets, harpoons, vision-based navigation (VBN) systems, and dragsails [22]. However, these are not suitable for a mission for the collection of multiple particles, which may undergo a re-entry phase for sample analysis, unlike the Earth debris removal operations, which deorbit. Although attractive, a robot-based on-orbit service (OOS) may cause the problem of attitude disturbance in the spacecraft base when the robotic arm physically intercepts the target particle, causing destabilization or severe hardware damage [23]. Although these problems can be partially overcome through the reaction-null space concept introduced by Yoshida and Nenchev [24], this solution remains unsuitable for the capture of multiple particles simultaneously, considering the wide size range of the ejecta.

Therefore, for the analyzed scenario, aerogel capture is the most suitable technology, which has already been used in the Stardust-NExT mission [25] and has been improved for the Tanpopo Cosmic Dust Collector mission [26]. This capture mechanism is based on the use of silica aerogel. It is the world's lightest solid. It consists of 99.8% air and is an ultra-low-density material. This is a fundamental property because, for the same internal structure, a lower density yields lower pressure shock levels upon impact [27].

Furthermore, this highly porous material based on silicon dioxide has a mesostructure similar to strings of pearls with sizes ranging from 10 to 100 Å, which also provides high emissivity to the material, enabling it to dissipate heat. It also circumvents issues related to the thermal cycles of the space environment [27]. The aerogel has also been used as a lightweight thermal insulator in one of the Mars Pathfinder rovers. This technology, unlike previous technologies, enables intact particle capture, preserving, therefore, not only the particle's elemental composition but also its structural phases, morphology, and chemical isotopic composition [27]. The aerogel gradually slows down the colliding particles, preventing the vaporization or melting of the sample. However, the dissipation of energy caused by their interaction increases the temperature, melting the aerogel around the particle and trapping it inside the mesostructure. To date, this has been achieved by creating aerogel tiles comprising two layers with densities of 0.01 and 0.03 g/cm^3 [28]. The top layer of the panel has a lower density and is designed to minimize the initial impact shock, whereas the dense layer can stop the most energetic particles from colliding with the aerogel panel. This configuration enables the capture of particles with a wider energy range without the need to increase the panel thickness to stop them [28]. To estimate the preliminary sizing of the panel's thickness, a relation between track length and aerogel density derived by Burchell *et al.* [29] can be used. Considering the mean density between the layers to be the aerogel density (i.e., 20 kg/m^3), the track length divided by the ejecta diameter was found to be ∼182.64①. Following this approach, the estimated track length enabling the collection of the largest particles was $l = 3.6528$ m. However, the NASA/JPL Return Capsule press-kit② states that the track created by an impacting particle can reach up to 200 times its dimensions. As Stardust-NeXT was expected to collect particles within a size range similar to that considered in this study, the ratio of ∼182.64 was assumed to be appropriate. In our case, $l = 4$ m was obtained, which is close to the value found in Ref. [29].

However, these data were obtained for different sizes and impact velocities (5–6 km/s), indicating that these values are clearly understood. Therefore, for effective and efficient capture, laboratory simulations and parametric analysis should be performed.

Another important feature of aerogels is the transparency of the media. This allows easy localization and removal of captured particles, tasks that can be considered as important as capturing itself because not finding a captured particle is equivalent to no capture at all. Localizing μm–mm-sized particles on a sufficiently wide collection surface is a cumbersome task. With an opaque medium, this becomes nearly impossible. Another main aspect of such a collection strategy is its simplicity. As aerogel capture is a passive technique, it does not

① To obtain this value, the open-source *WebPlotDigitizer* available online was used.
② https://www.jpl.nasa.gov/missions/stardust

require precision pointing, mechanisms for warming up, or any other devices [27]. This results in the high reliability of the technology.

Once in position, similar to the Stardust-NeXT, the spacecraft extends a tennis-racket-shaped catcher filled with aerogel for particle capture. After capturing the ejecta, this device folds down into a return capsule, enclosing the sample for safe delivery to the Earth. This device is linked to a holder rather than being directly in contact with the aerogel. It should be designed according to the dimensions of the aerogel panel and must maximize the exposure area. The most widely used approach is to fabricate a body case with aluminum alloy A7075 in the shape of a gridded lid [26]. Tabata *et al.* [26] reported that for an aerogel of dimensions 92 mm × 92 mm, the final exposure area was approximately 56 cm^2. Thus, the holder covered about 33.84% of the aerogel surface. This implies that if, as in the case of Stardust-NeXT, the desired exposure area is approximately 1040 cm^2, then the catcher's surface area considering the holder size should be ∼1392 cm^2. In any case, the panel area, and therefore the exposure area, is one of the main aspects that affects the time required for particle collection. Therefore, a parametric analysis was also be conducted for this case.

Overall, the main advantages of the use of aerogel for this type of in-orbit capture are:

- It is an already-tested and space-proven technology.
- It passed both pressurization/re-pressurization and vibration tests [26].
- Due to its mesostructure, aerogel has high emissivity. It therefore does not trap heat and is insensitive to the thermal cycles of the space environment.
- Its transparency allows the traceability of trapped particles, which can then be detected and extracted with relative ease.
- Aerogel capture is relatively simple and, therefore, improves the simplicity and reliability of particle capture.
- Being inorganic, aerogel is impervious to radiation and ionic erosion [27].
- As it has an ultra-low density, even for a very large collector, no mass constraints will arise.
- Aerogel enables intact particle capture, preserving the particles' elemental composition, structural phases, morphology, and chemical isotopic composition.

However, aerogels have never been used at this range of velocities. In fact, it has generally been used to stop cosmic dust from impacting with hypervelocities (km/s). In this mission scenario, with the assumptions discussed earlier, the velocities considered are one order of magnitude lower. The capture efficiency under these conditions must be proven.

7 Conclusions

The presented study aims at verifying the feasibility of performing an in-orbit sample collection of asteroids' material. This is crucial for future space exploration and resource utilization. In this regard, this study improves the characterization of bouncing behavior, enlarges the studied area to the neighborhood of L_2, and presents a global view of a mission scenario, from physical dynamics to the satellite's capture mechanism.

Concerning the bouncing behavior, the original approach for obtaining the restitution coefficients can better characterize the nature of the ejecta's trajectories. Previous studies, such as those of Latino *et al.*, showed that an almost evenly distributed number of particles impact the asteroid, including particles after a previous rebound or those injected into orbit around the celestial body after an impact. However, this scenario is unlikely. The improved approach, however, can model a scenario in which the sample trajectories are better distributed according to their final fates. This was achieved by limiting the impact angles and allowing a rebound from the asteroid by introducing the *OutRange* and $OutRange_{\mathrm{reb}}$ categories. As an improvement over previous studies, this strategy blocks a majority of trajectories arising from unfeasible rebounds, as evidenced by the number of rebounds, which dropped from 522,349 to 131,853. As a result, the $Impact_{\mathrm{reb}}$ and $Orbit_{\mathrm{reb}}$ categories became less populated.

Furthermore, this study aimed to investigate the neighboring zones of L_2. The enlarged region of interest obtained by considering $C' = 0.9999999999997C_2$ brought to light several sample trajectories that could escape. Their number was 16,610. This number does not change in either the point mass or rigid body approximation because it does not depend on the number of collisions. Furthermore, particles with $\theta < 100°$ and $200° < \theta < 350°$ could escape. Thus, two distinct groups of initial conditions that allow a particle to leave the system were identified. For both groups, the number of escaping orbits increased with size. Interestingly, no

particles with $r_P = 78.5$ μm were found to leave Ryugu. This behavior can be attributed to the value chosen for C'. By studying how γ_{ej} affects this behavior, the best conditions that allow a particle to escape were found to be those that cause the particle to eject toward the bottleneck. However, the succession of eclipses, that is, the time when $\beta = 0$, has not been considered. This can possibly significantly change the dynamics.

The other key parameter that affects the feasibility of the proposed capture strategy is the time required to perform the collection. To quantify it, the mass collected by Hayabusa2 [21] was considered the mass threshold value to be captured. After 22.48 days, the mission could gather the required number of samples. Specifically, it collected 1.8040 g and 3.458 g from particles with $r_P =$ 1.181 mm and $r_P = 2.283$ mm, respectively.

The proposed mechanism for the capture strategy uses silica-based aerogel technology. To estimate its initial size, the capture velocity was assumed to be the velocity of the escaped ejecta at $t =$ tof. Although this hypothesis was adopted to simplify the problem, it could successfully estimate the ejecta velocity when they leave Hill's sphere through L_2. This is fundamental information required by satellites to capture particles. The capture velocity was found to be between 100 and 300 m/s, corresponding to a maximum kinetic energy of $E_{\mathrm{kin}_{\max}} = 1.9258 \times 10^{-4}$ J. Currently, the velocity considered is only that of the ejecta, but future research should investigate the effect of using the relative speed between the satellite and the particle. Note that even though only ejecta with $r_P \leqslant 2.283$ mm were expected to be captured, the maximum kinetic energy value corresponds to a particle with $r_P = 10$ mm, based on a conservative approach. However, the most conservative approach need not be applied. Based on the reference trends reported in Refs. [26] and [29], the required minimum thickness and surface area of the aerogel tiles were found to be 4 m and 1392 cm^2, respectively. However, these values should be determined by considering the specific conditions of each scenario through simulations. In conclusion, even under simplifying assumptions, the feasibility of the sample collection of an in-orbit asteroid by means of a satellite orbiting around the second libration point could be assessed. Among these assumptions, the strongest hypothesis adopted is regarding the time of capture of the particle, which was assumed to be the same as that of the particle's escape from Hill's sphere. This situation is unlikely to occur. Although this could have a major impact on the capture mechanism, the main contribution of this study is the ejecta dynamics coupled with the bouncing characterization. Future research should investigate the effect of relaxing this assumption, which in turn is expected to improve the preliminary sizing of the aerogel panel. This can be studied based on trends derived from impacts occurring at velocities of different orders of magnitude than those considered in this study. Moreover, the effect of considering the relative velocity between the spacecraft and ejecta should be investigated.

Nevertheless, using an aerogel-based capture strategy, the proposed mission could collect 5.262 g of Ryugu's ejecta in 22.48 days from the time of the arrival of the spacecraft at the asteroid, thus validating the feasibility of such a sample capture mission.

Appendix A

In this appendix, a flow chart of the code used to build the database containing the ejecta's initial and final conditions, time of flight, and final fate is shown in Fig. A1. Its color-coding is as follows: the starting and final blocks are colored green and red, respectively, and the particle's fate is assessed in the blocks colored blue.

Appendix B

Figure A2 shows the database built using the method proposed in this paper. Only the PM-TDM1 scenario is reported, as it was chosen as the most representative solution. As shown in the figure, the database's dimensions are 387,830 × 9, but only a few initial lines are shown for brevity. The purpose of Fig. A2 is to show the structure of the database. The size is r_P; Long and Long_imp are θ and θ_{imp}, respectively; Gamma and Gamma_imp are γ and γ_{imp}, respectively; and Escape categorizes the ejecta's final fate. The categories introduced in the text are represented as follows: OR denotes OutRange; N denotes Impact; N_reb denotes Impact_reb; Orbit_reb denotes Orbit_reb; and OR_reb denotes OutRange_reb.

Acknowledgements

This project received funding from the European Union's Horizon 2020 research and innovation program under the

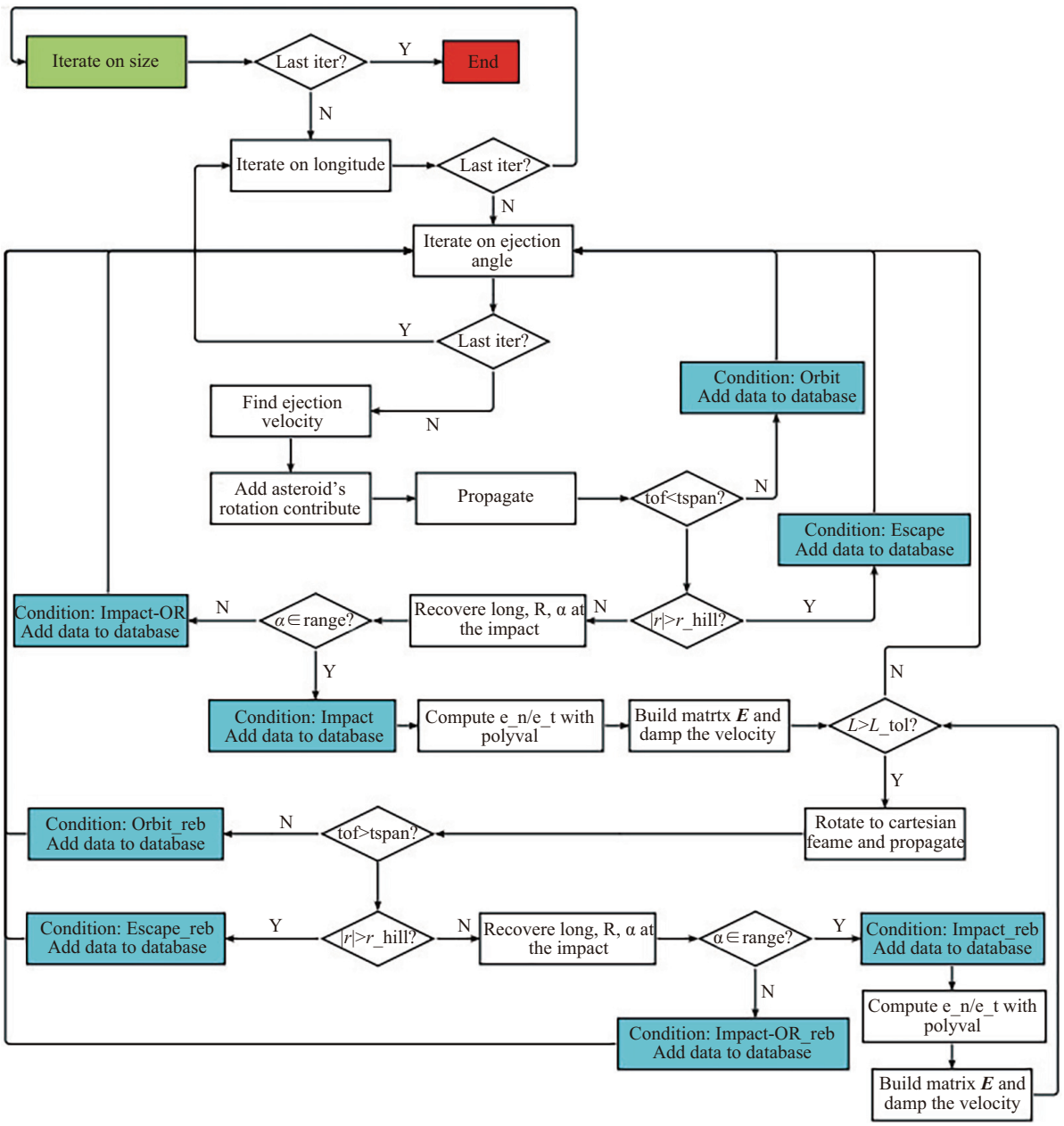

Fig. A1 Block diagram of the database code. Green represents the starting block, and red marks the final one. The blocks in which the final condition of the ejecta is assessed are shown in blue. The final condition is then added to the database.

387830x9 string

	1	2	3	4	5	6	7	8	9
1	Size [mm]	Long [°]	V_ej [cm/s]	Gamma [°]	Long_imp [°]	V_imp [cm/s]	Gamma_imp [°]	tof [days]	Escape
2	0.0011809	0	35.7642	-65	322.3625	35.7149	-79.5428	1.7333	OR
3	0.0011809	0	35.7642	-64	316.8493	35.7166	-81.5843	1.7527	OR
4	0.0011809	0	35.7642	-63	311.3214	35.7185	-83.637	1.773	OR
5	0.0011809	0	35.7642	-62	305.7732	35.7206	-85.7025	1.7942	OR
6	0.0011809	0	35.7642	-61	300.1959	35.7228	-87.7848	1.8165	OR
7	0.0011809	0	35.7642	-60	294.5869	35.7252	-89.8838	1.8398	OR
8	0.0011809	0	35.7642	-59	288.9378	35.7277	87.9971	1.8641	OR
9	0.0011809	0	35.7642	-58	283.2413	35.7304	85.8554	1.8896	OR
10	0.0011809	0	35.7642	-57	277.4926	35.7331	83.6897	1.9162	OR
11	0.0011809	0	35.7642	-56	271.6835	35.7359	81.4974	1.9441	OR
12	0.0011809	0	35.7642	-55	274.1929	35.7387	87.662	1.9732	OR
13	0.0011809	0	35.7642	-54	280.1488	35.7415	-82.6812	2.0036	OR
14	0.0011809	0	35.7642	-53	286.1873	35.7443	-72.8925	2.0355	OR
15	0.0011809	0	35.7642	-52	292.3221	35.7471	-62.95	2.0687	OR
16	0.0011809	0	35.7642	-51	298.5651	35.7498	-52.834	2.1036	OR
17	0.0011809	0	35.7642	-50	304.9246	35.7524	-42.5301	2.14	N
18	0.0011809	304.9246	6.4206	9.1946	5.3408	2.3524e-06	-0.4768	0.0096758	N_reb
19	0.0011809	5.3408	1.1187	57.8211	NaN	NaN	NaN	90	Orbit_reb
20	0.0011809	0	35.7642	-49	311.4176	35.7549	-32.0104	2.1781	N
21	0.0011809	311.4176	5.42	40.2059	5.4777	1.9872e-06	-0.74311	0.0062795	N_reb
22	0.0011809	5.4777	0.97585	9.1096	NaN	NaN	NaN	90	Orbit_reb
23	0.0011809	0	35.7642	-48	318.0543	35.7571	-21.257	2.218	N
24	0.0011809	318.0543	9.0184	74.7502	5.6178	3.3047e-06	-1.0649	0.0039244	OR_reb
25	0.0011809	0	35.7642	-47	324.8595	35.7592	-10.2305	2.2599	N
26	0.0011809	324.8595	24.8913	87.7819	6.2831	9.1191e-06	0.038483	0.012654	OR_reb

Fig. A2 A part of the database built following the procedure reported in this work is shown in this figure for PM-TDM1. Specifically, the size is r_P; Long and Long_imp are θ and θ_{imp}, respectively; Gamma and Gamma_imp are γ and γ_{imp}, respectively; and Escape categorizes the ejecta's final fate. The categories introduced in the text are represented as follows: OR denotes OutRange; N denotes Impact; N_reb denotes Impact_reb; Orbit_reb denotes Orbit_reb; and OR_reb is OutRange_reb.

Marie Sklodowska-Curie grant agreement No. 896404-CRADLE and from the European Research Council (ERC) under the European Union's Horizon 2020 Research and Innovation Program (grant agreement No. 679086–COMPASS).

Funding note

Open access funding provided by Politecnico di Milano within the CRUI-CARE Agreement.

Declaration of competing interest

The authors have no competing interests to declare that are relevant to the content of this article.

References

[1] Xie, R., Bennett, N. J., Dempster, A. G. Target evaluation for near earth asteroid long-term mining missions. *Acta Astronautica*, **2021**, 181: 249–270.

[2] Hein, A. M., Matheson, R., Fries, D. A techno-economic analysis of asteroid mining. *Acta Astronautica*, **2020**, 168: 104–115.

[3] Watanabe, S. I., Tsuda, Y., Yoshikawa, M., Tanaka, S., Saiki, T., Nakazawa, S. Hayabusa2 mission overview. *Space Science Reviews*, **2017**, 208(1): 3–16.

[4] Turconi, A. Modelling small bodies gravitational potential for autonomous proximity operations. Ph.D. Thesis. University of Surrey, **2018**.

[5] Rumford, T. E. Demonstration of autonomous rendezvous technology (DART) project summary. In: Proceedings of the SPIE 5088, Space Systems Technology and Operations, **2003**.

[6] Trisolini, M., Colombo, C., Tsuda, Y. Ejecta dynamics around asteroids in view of in-orbit particle collection missions. In: Proceedings of the 72nd International Astronautical Congress, **2021**: IAC-21-C1.6.5-x65610.

[7] Villegas-Pinto, D., Soldini, S., Tsuda, Y., Heiligers, J. Temporary capture of asteroid ejecta into periodic orbits: Application to JAXA's Hayabusa2 impact event. In: Proceedings of the AIAA Scitech 2020 Forum, **2020**: AIAA 2020-0221.

[8] Latino, A., Soldini, S., Colombo, C., Tsuda, Y., *et al.* Ejecta orbital and bouncing dynamics around asteroid Ryugu. In: Proceedings of the 70th International Astronautical Congress, **2019**.

[9] Kikuchi, S., Ogawa, N., Mori, O., Saiki, T., Takei, Y., Terui, F., Ono, G., Mimasu, Y., Yoshikawa, K., Van Wal, S., *et al.* Ballistic deployment of the Hayabusa2 artificial landmarks in the microgravity environment of Ryugu. *Icarus*, **2021**, 358: 114220.

[10] Soldini, S., Tsuda, Y. Assessing the hazard posed by Ryugu ejecta dynamics on Hayabusa2 spacecraft. In: Proceedings of the 26th International Symposium of Space Flight Dynamics, **2017**.

[11] Gustafson, B. A. S. Physics of zodiacal dust. *Annual Review of Earth and Planetary Sciences*, **1994**, 22: 553–595.

[12] Soldini, S. Design and control of solar radiation pressure assisted missions in the Sun–Earth restricted three-body problem. Ph.D. Thesis. University of Southampton, **2016**.

[13] Dell'Elce, L., Baresi, N., Naidu, S. P., Benner, L. A. M., Scheeres, D. J. Numerical investigation of the dynamical environment of 65803 Didymos. *Advances in Space Research*, **2017**, 59(5): 1304–1320.

[14] Latino, A. Ejecta orbital and bouncing dynamics around asteroid Ryugu. M.Sc. Thesis. Politecnico di Milano, **2019**.

[15] Villegas-Pinto, D., Soldini, S., Tsuda, Y., Heiligers, J. Temporary capture of asteroid ejecta into periodic orbits: Application to JAXA's Hayabusa2 impact event. In: Proceedings of the AIAA Scitech 2020 Forum, **2020**: AIAA 2020-0221.

[16] García Yárnoz, D., Sánchez Cuartielles, J. P., McInnes, C. R. Passive sorting of asteroid material using solar radiation pressure. *Journal of Guidance Control Dynamics*, **2014**, 37(4): 1223–1235.

[17] Koon, W. S., Lo, M. W., Marsden, J. E., Ross, S. D. Dynamical systems, the three-body problem and space mission design. In: *Equadiff 99*. World Scientific Publishing Company, **2000**: 1167–1181.

[18] Yu, Y., Michel, P., Schwartz, S. R., Naidu, S. P., Benner, L. A. M. Ejecta cloud from the AIDA space project kinetic impact on the secondary of a binary asteroid: I. mechanical environment and dynamical model. *Icarus*, **2017**, 282: 313–325.

[19] Trisolini, M., Colombo, C., Tsuda, Y. Target selection for Near-Earth Asteroids in-orbit sample collection missions. *Acta Astronautica*, **2023**, 203: 407–420.

[20] Conley, C. C. Low energy transit orbits in the restricted three-body problems. *SIAM Journal on Applied Mathematics*, **1968**, 16: 732–746.

[21] Yada, T., Abe, M., Okada, T., Nakato, A., Yogata, K., Miyazaki, A., Hatakeda, K., Kumagai, K., Nishimura, M., Hitomi, Y., *et al.* Preliminary analysis of the Hayabusa2 samples returned from C-type asteroid Ryugu. *Nature Astronomy*, **2022**, 6: 214–220.

[22] Forshaw, J. L., Aglietti, G. S., Salmon, T., Retat, I., Burgess, C., Chabot, T., Pisseloup, A., Phipps, A., Bernal, C., Chaumette, F., Pollini, A., Steyn, W. The RemoveDebris ADR mission: Preparing for an international space station launch. In: Proceedings of the 7th European Conference on Space Debris, **2017**.

[23] Flores-Abad, A., Zhang, L., Wei, Z., Ma, O. Optimal capture of a tumbling object in orbit using a space manipulator. *Journal of Intelligent & Robotic Systems*, **2017**, 86: 199–211.

[24] Yoshida, K., Nenchev, D. N. Space robot impact analysis and satellite-base impulse minimization using reaction null-space. In: Proceedings of the IEEE International Conference on Robotics and Automation, **1995**: 1271–1277.

[25] Don, B. The stardust mission: Analyzing samples from the edge of the solar system. *Annual Review of Earth and Planetary Sciences*, **2014**, 42: 179–205.

[26] Tabata, M., Imai, E., Yano, H., Hashimoto, H., Kawai, H., Kawaguchi, Y., Kobayashi, K., Mita, H., Okudaira, K., Sasaki, S., *et al.* Design of a silica-aerogel-based cosmic dust collector for the tanpopo mission aboard the international space station. *Transactions of the Japan Society for Aeronautical and Space Sciences, Aerospace Technology Japan*, **2014**, 12(ists29): Pk_29–Pk_34.

[27] Tsou, P. Silica aerogel captures cosmic dust intact. *Journal of Non-Crystalline Solids*, **1995**, 186: 415–427.

[28] Tabata, M., Yano, H., Kawai, H., Imai, E., Kawaguchi, Y., Hashimoto, H., Yamagishi, A. Silica aerogel for capturing intact interplanetary dust particles for the tanpopo experiment. *Origins of Life and Evolution of Biospheres*, **2015**, 45: 225–229.

[29] Burchell, M. J., Graham, G., Kearsley, A. Cosmic dust collection in aerogel. *Annual Review of Earth and Planetary Sciences*, **2006**, 34: 385–418.

Carlo Burattini is a space engineer graduated from Politecnico di Milano in 2022, with his master thesis in asteroid exploration and sample collection. He is currently a space system engineer working in different cutting-edge microsatellite deep space missions to study space weather and planetary defence rapid reconnaissance. His main research interests include space mission analysis and design, feasibility assessment, and concurrent design studies.

Camilla Colombo is an associate professor in orbital mechanics at Politecnico di Milano and principal investigator of the COMPASS project. Before that, she was an associate professor and lecturer in spacecraft engineering at the University of Southampton in the Astronautics Research Group till July 2016. Her research areas spaces among orbital dynamics, trajectory design and optimisation, dynamical system analysis and control, and space mission analysis and design.

She is delegate for the Inter Agency Debris Coordination Committee and the UN mandated Space Mission Planning Advisory Group for mission to asteroids.

Mirko Trisolini holds his Ph.D. degree in aerospace engineering from the University of Southampton since 2018 and was a postdoctoral associate at Politecnico di Milano. He was awarded a Marie-Curie Global Fellowship in 2020 by the European Union for his research on orbital dynamics and mission design. He has published 16 scientific papers on orbital dynamics and optimisation and he is currently an astrodynamics specialist at Vyoma GmbH. His research interests are in the field of orbital dynamics, mission design, space situational awareness, and optimization.